

Surface and structural characterization of $Ce_xZr_{1-x}O_2$ CEZIRENCAT mixed oxides as potential three-way catalyst promoters

G. Colón,^{a†} M. Pijolat,^{*a} F. Valdivieso,^a H. Vidal,^{b‡} J. Kašpar,^b E. Finocchio,^{c§} M. Daturi,^{c§} C. Binet,^c J. C. Lavalley,^c R. T. Baker^d and S. Bernal^d

^a Centre SPIN, Ecole Nationale Supérieure des Mines, 158, Cours Fauriel, 42023 St. Etienne Cedex-2, France. E-mail: mpijolat@spin.emse.fr

^b Dipartimento di Scienze Chimiche, Università di Trieste, Via Giorgieri, 1, 34127 Trieste, Italy

^c Laboratoire de Catalyse et Spectrochimie, UMR 6506, ISMRA, 6, Bd du Maréchal Juin, 14050 Caen Cedex, France

^d Departamento de Ciencia de Materiales, Ingeniería Metalúrgica y Química Inorgánica, Facultad de Ciencias, Universidad de Cádiz. Apdo. 40, Puerto Real, 11510 Cádiz, Spain

Received 20th July 1998, Accepted 2nd October 1998

The textural and structural properties of high specific surface area (HS) $Ce_xZr_{1-x}O_2$ mixed oxides (CeZrMO) and their modification upon thermal aging have been investigated. Results from BET area determination and complete porosity analysis, as well as high-resolution electron microscopy, XRD, Raman and FTIR spectroscopies are presented. Some relationships between the molar composition of the binary systems and their textural and structural properties are presented. In addition, it has been possible to propose an explanation for structural features of the mixed oxides (solid-solution structures and possible phase segregation) as a function of Ce content, a point of great interest for the knowledge of phase composition and stability of CeZrMO.

Introduction

Ceria-containing materials are widely employed as promoters for noble metal/alumina automotive three-way catalysts (TWCs). The suggested promoting roles for CeO_2 are the stabilization of metal dispersion on the alumina support, it is thought to decrease the intense sintering which may occur in the monolithic converter,¹ the promotion of the water-gas shift reaction and the improvement of the oxygen storage/release capacity (OSC) by shifting between Ce^{4+} and Ce^{3+} ^{2,3} under reductive and oxidative conditions. These latter redox properties are strongly affected and enhanced by introducing foreign cations such as Zr, Gd or Tb⁴⁻⁷ into the CeO_2 lattice to form a solid solution. The increase in oxygen storage/transport and redox capacities is the result of enhanced oxygen ion mobility within the crystal lattice,^{8,9} originating from formation of a defective solid solution, in which the smaller Zr^{4+} (ionic radius 0.84 Å) has replaced some cerium cations (0.96 Å). Recently, a new generation of TWCs containing mixed oxides of CeO_2 and ZrO_2 has been developed. These show good thermal resistance,^{10,11} in addition to the above-mentioned improvements in redox properties. This high thermal stability is an essential requirement for the CeO_2 -containing supports since a close-coupled converter, positioned near to the engine, is often employed in automotive applications and the TWCs can experience temperatures up to

1273 K. Therefore, the surface and structural characterization of CeZrMO of potential use as TWC promoters is of great relevance.

The formation of a CeO_2 - ZrO_2 solid solution has been claimed to increase the thermal stability of CeO_2 against sintering and to improve the OSC. A recent study showed that the cumulative OSC is independent of the specific surface area, even at moderate temperatures.⁹ There are several points concerning these advanced materials that must be clarified in order to provide a sound scientific basis for the development of the next generation of TWCs: dependence of textural properties on composition; effect of aging on redox properties; effect of phase stability on aging. Several papers have reported on the characterization and catalytic behaviour of a few compositions while, with the exception of a previous paper in which the redox behaviour of highly sintered CeZrMO⁹ was investigated, no systematic studies on different compositions and textures have appeared so far. With the aim of providing insight into these systems we have recently established a network^{||} of different laboratories and started a systematic investigation of a number of HS and LS CeZrMO.

In the present paper, $Ce_xZr_{1-x}O_2$ ($0 \leq x \leq 1.0$) mixed oxides of high specific surface area (HS), and HS samples which had been thermally aged to obtain the corresponding low specific surface area (LS) series, were characterised. The relationships between the textural and structural properties and the Ce/Zr ratio are investigated by means of different techniques.

[†] On leave from Instituto de Ciencia de Materiales-CSIC, Adva, Americo Vespucio s/n, Isla de la Cartuja, 41092 Sevilla, Spain.

[‡] On leave from Departamento de Ciencia de los Materiales e Ingeniería Metalúrgica y Química Inorgánica, Universidad de Cádiz, Puerto Real, 11510, Spain.

[§] On leave from the Istituto di Chimica, Facoltà di Ingegneria, Università di Genova, P. le J. F. Kennedy, 16129 Genova, Italy.

^{||} CEZIRENCAT network is supported by the European Union Training and Mobility of Researcher (TMR) Program, home page: <http://www.dschi.univ.trieste.it/cezirencat>.

Experimental

HS ceria–zirconia mixed oxides with different molar compositions were synthesized by Rhône-Poulenc using a precipitation route from nitrate precursors. Hereafter they will be referred to as CZ XX/YY HS, where XX and YY indicates the molar percentage of CeO₂ and ZrO₂, respectively. LS mixed oxides were obtained by submitting the HS samples to calcination in air at 1173 K for 140 h in the presence of water vapour.

The specific surface area (S_{BET}) measurements and surface characterization were performed by the BET method using N₂ adsorption/desorption at 77 K (Micromeritics 2100E).

XRD spectra were recorded on a Siemens D501 diffractometer (Cu-K α) which could be equipped with a high-temperature cell. Acquisition conditions were: $2\theta = 15^\circ$ – 75° , step size 0.006° and counting time 5 s. The goniometer angular error of the apparatus was $\Delta\theta = \pm 0.005^\circ$ and the corresponding error value for d_{hkl} was not higher than 3%. Indexation and calculation of unit cell parameters were carried out by using the intensities of lines (111) of CeO₂, Ce_xZr_{1-x}O₂ ($x > 0.5$), (101) of Ce_xZr_{1-x}O₂ ($x \leq 0.5$) and finally ($\bar{1}11$) and (101) of ZrO₂ (monoclinic and tetragonal, respectively). For calculation of the unit cell parameters, the tetragonal relationship of d_{hkl} and the cell parameters

$$\frac{1}{d_{hkl}^2} = \frac{h^2 + k^2}{a^2} + \frac{l^2}{c^2}$$

was assumed for all samples.

The mean crystal size, D , was calculated from the Warren and Averbach equation, assuming a Gaussian fitting of peaks (peaks were fitted by using a Voigt function),

$$D = \frac{\lambda 180}{\pi \cos \theta \sqrt{L^2 - L_{\text{Ref}}^2}}$$

L and L_{Ref} being the full width at half maximum (FWHM) of the sample and a reference material, respectively. The reference powder was prepared by annealing a CZ 100/0 HS sample at 1473 K for 140 h, followed by slow cooling to room temperature.

The density of the samples was measured by the pycnometry technique using a Micromeritics ACCUPYC 1330.

The oxide samples were studied by transmission electron microscopy/high-resolution electron microscopy (TEM/HREM) using a JEOL 2000-EX instrument. The microscope was equipped with a top-entry specimen holder and ion pumping system, operated at an accelerating voltage of 200 kV and gave a nominal structural resolution of 0.21 nm. Samples were prepared by dipping a 3 mm holey carbon copper grid into an ultrasonic dispersion of the oxide powder in hexane. Selected area electron diffraction (SAED) patterns and high-resolution micrographs over a range of magnifi-

cations up to $\times 600\text{K}$ were recorded. All diffractogram and micrograph negatives were developed chemically and then digitised, processed and analysed using the SEMPER 6+ software package. High-resolution micrographs in which the internal crystal structure was well defined were used to generate digital diffraction patterns (DDPs).

The Raman spectra were measured on a Perkin Elmer 2000 FT-Raman instrument with a diode-pumped YAG laser and a room-temperature super InGaAs detector. The laser power was 100–500 mW.

For the IR studies the powders were pressed into self-supported wafers of *ca.* 10 mg cm⁻² and activated *in situ*, in a quartz cell placed into the IR beam, by heating steps under O₂ up to 873 K, followed by evacuation at the same temperature. Methanol was introduced at room temperature onto the activated samples and then the system was evacuated. IR spectra were recorded at room temperature (rt) with a Nicolet Magna 550 FTIR spectrometer (resolution 4 cm⁻¹) after quenching the samples to room temperature. The reported spectra are those of methoxy species subtracted from that of the substrate, *i.e.* before methanol adsorption. The spectra have been treated using the Nicolet OMNICTM software.

Compared to the IR spectroscopy, which gives a quantitative estimation of the methoxy species adsorbed on zirconium or cerium ions, X-ray photoelectron spectroscopy (XPS) would not give significant additional information on the surface composition of the mixed oxides.

Results and discussion

Textural properties

The specific surface areas of all the HS and LS samples are reported in Table 1. They range from *ca.* 95 to 100 m² g⁻¹ for the HS series, and from 15 to 30 m² g⁻¹ for the LS series. Note that, after the same annealing treatment, the highest S_{BET} , 110 m² g⁻¹ for CZ 80/20, decreases to the lowest value, 15 m² g⁻¹. This is in agreement with previous studies on the thermal stability of Ce_xZr_{1-x}O₂ solid solutions with $0 < x < 0.36$.¹² In Fig. 1.1–1.3 the adsorption/desorption isotherms for some of the Ce_xZr_{1-x}O₂ HS mixed oxides are reported. In all cases the isotherms are of type IV according to BDDT classification.¹³ According to the IUPAC classification,¹³ the hysteresis loops are close to the H1 type for the CZ 100/0 sample, while for the binary systems the hysteresis loop progresses from H2 type for CZ 80/20 to H1 as the Ce content decreases. A hysteresis loop of type H1 is usually related to open tubular pores with circular or polygonal sections meanwhile H2 indicates the presence of pores with ill defined size and shape. Mixed oxides from LS series (Fig. 2.1–2.3) also present adsorption isotherms of type IV, but in this case the hysteresis loops are significantly reduced, indicating a great reduction of the pores system. In all cases, the hysteresis

Table 1 Results of the textural analysis by N₂ adsorption/desorption for Ce_xZr_{1-x}O₂

	Sample	$S_{\text{BET}}/\text{m}^2 \text{ g}^{-1}$	$S_v/\text{m}^2 \text{ g}^{-1}$	C_{BET}	Cumulative pore volume/cm ³ g ⁻¹	$V_{\text{micro}}/\text{cm}^3 \text{ g}^{-1}$	Average pore diameter/Å
HS	CZ 100/0	100	94	117	0.2036	0.0020	65
	CZ 80/20	111	105	71	0.2119	0.0003	40
	CZ 68/32	100	97	110	0.2588	0.0007	65
	CZ 50/50	106	99	99	0.2282	0.0018	55
	CZ 15/85	95	95	130	0.3241	0.0006	95
	CZ 0/100	53	52	—	0.1990	0.0001	30
LS	CZ 100/0	20	17	63	0.1615	0.0005	115
	CZ 80/20	15	14	52	0.1184	0.0000	250
	CZ 68/32	23	15	122	0.1670	0.0031	220
	CZ 50/50	21	17	77	0.1339	0.0010	250
	CZ 15/85	30	28	38	0.2080	0.0019	220

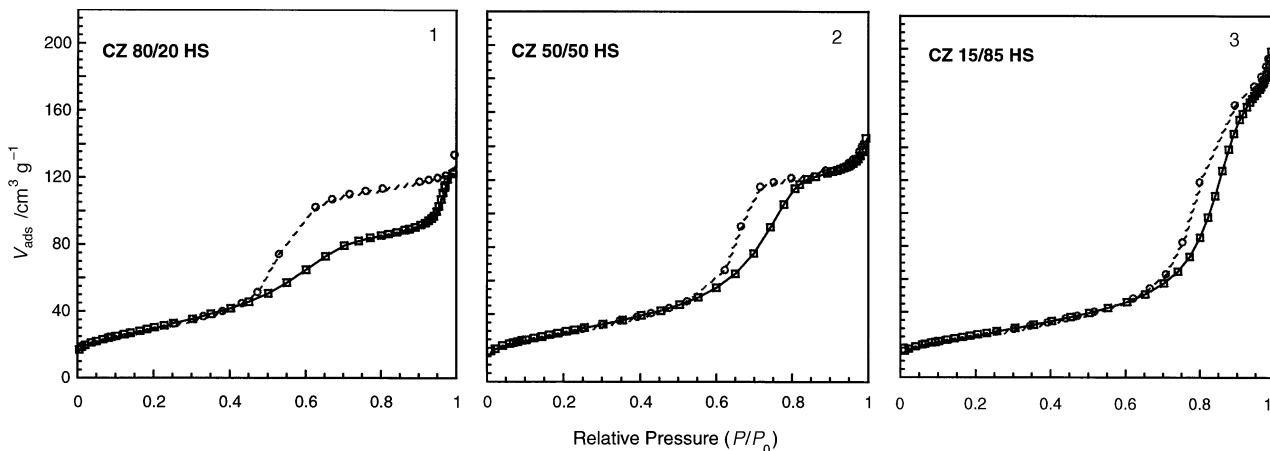


Fig. 1 Adsorption/desorption isotherms for CZ 80/20, 50/50 and 15/85 HS samples.

could be ascribed to type H1 and it does not change with Ce content.

By applying the BJH method^{13,14} to the desorption branch of the isotherm, we have obtained the pore-size distribution for the HS and LS samples (Fig. 3.1–3.3 and Fig. 4.1–4.3). The HS series presents quite a narrow distribution of pore diameter located between 40 and 65 Å with the exception of the CZ 15/85 HS (95 Å). In the LS series, the pore size shifts to higher values and the porous distribution is also wider than in the latter case. The *t*-plots (we show only the case of CZ 50/50 as a representative, Fig. 5.1–5.2), confirm the absence of signifi-

cant microporosity in both the HS and LS series ($V_{\text{micro}} < 1\%$ and $< 2\%$ of V_t for HS and LS, respectively). This is also supported by the isotherm shape at low relative pressure values. The data of the surface characterization from N_2 adsorption for all mixed oxides are summarized in Table 1.

Structural properties

The XRD patterns of the $Ce_xZr_{1-x}O_2$ are shown in Fig. 6 and 7. Generally speaking, the binary systems present typical diffraction patterns of $Ce_xZr_{1-x}O_2$ solid solutions. Note the shift

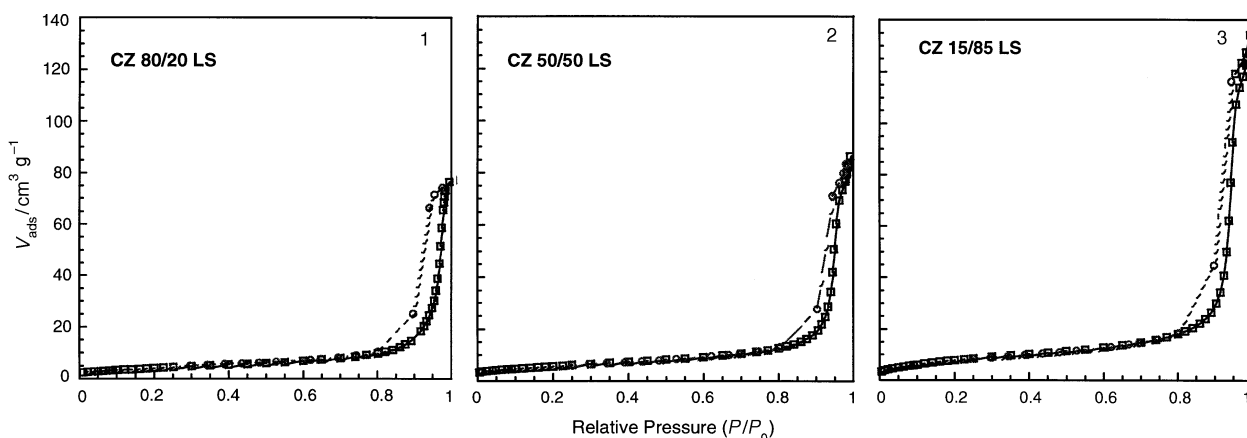


Fig. 2 Adsorption/desorption isotherms for CZ 80/20, 50/50 and 15/85 LS samples.

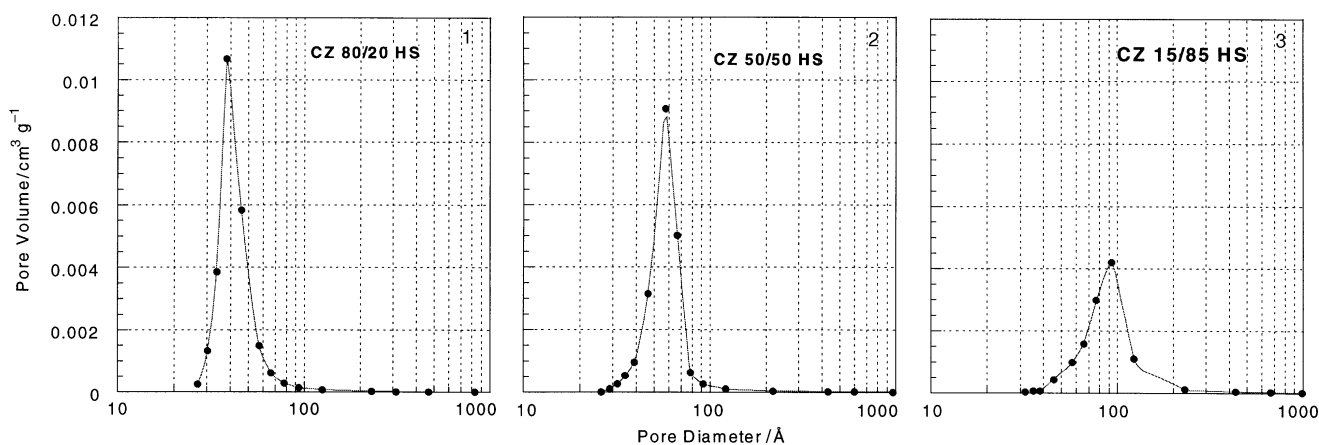


Fig. 3 Pore size distribution for CZ 80/20, 50/50 and 15/85 HS samples.

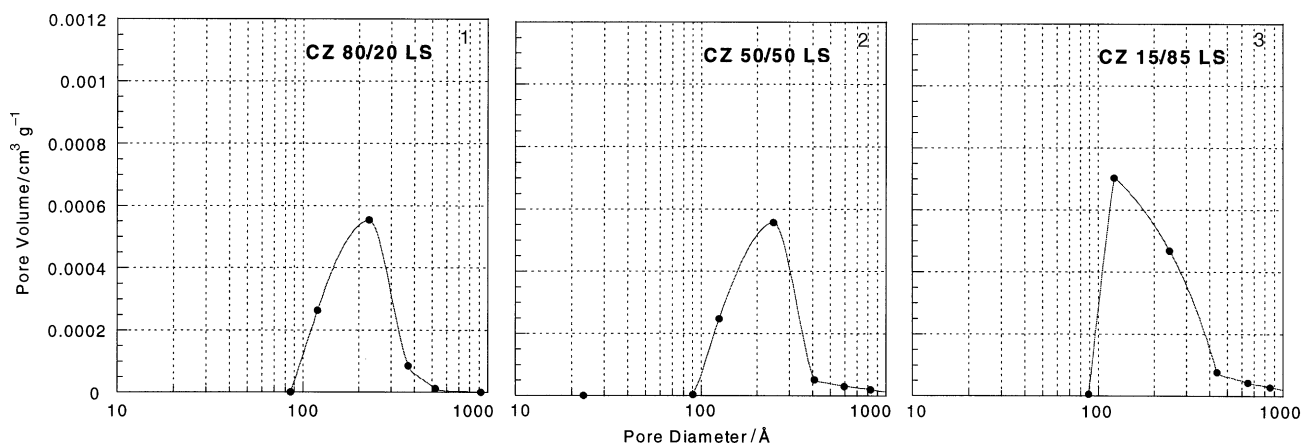


Fig. 4 Pore size distribution for CZ 80/20, 50/50 and 15/85 LS samples.

of the (111) peak (at $2\theta \approx 30^\circ$) with increasing ZrO_2 content, indicating a progressive substitution of the small Zr^{4+} (0.84 Å) for the large Ce^{4+} (0.97 Å) in the lattice. In the HS series, no diffraction peaks assigned to $m-ZrO_2$ or CeO_2 as segregated phases were detected, with the exception of the CZ 15/85 HS (the mixed oxide richest in Zr) which shows the presence of peaks attributable to $m-ZrO_2$ (ca. 30% from the main X-ray peak intensities ratio of ZrO_2 and solid solution, giving a solid solution with composition approximately $Ce_{0.2}Zr_{0.8}O_2$). This indicates a partial segregation/lack of insertion of the ZrO_2 from/into the solid solution. Remarkably, most of the $m-ZrO_2$ previously detected in this HS sample was incorporated into the lattice upon calcination, as noticed in the XRD pattern of the CZ 15/85 LS. Within the detection limit of the

technique we do not find evidence for the presence of $m-ZrO_2$. It appears that the calcination at 1173 K in the presence of water vapour favours ZrO_2 incorporation into the lattice. On the other hand a partial segregation of phases is observed in CZ 50/50 LS (Fig. 7). The CZ 50/50 LS XRD pattern shows

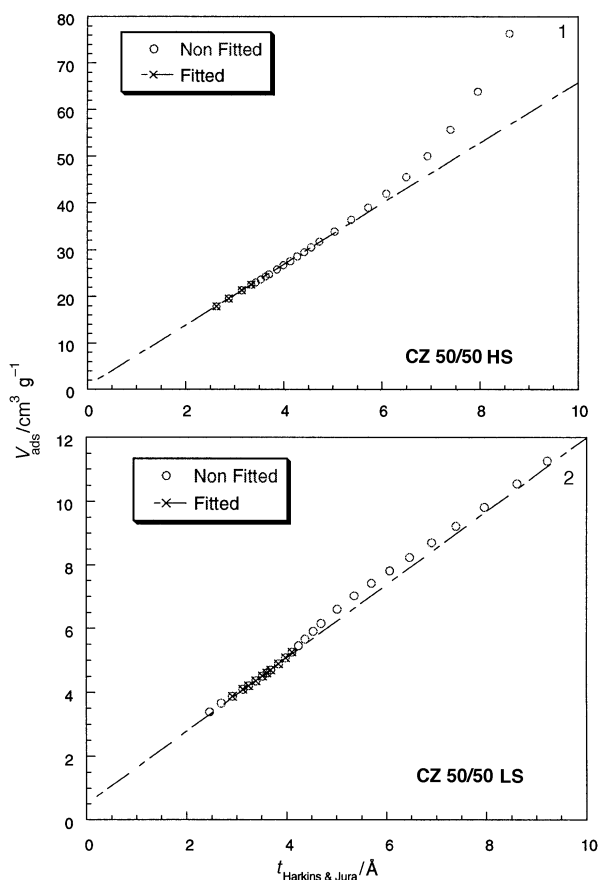


Fig. 5 t -Plots for CZ 50/50 HS and LS samples.

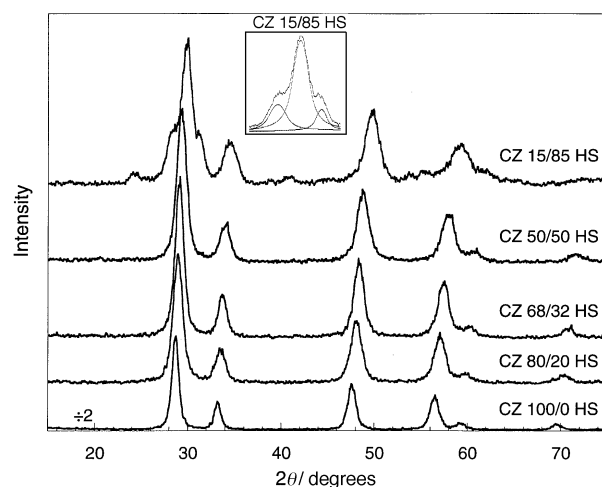


Fig. 6 XRD patterns for HS samples.

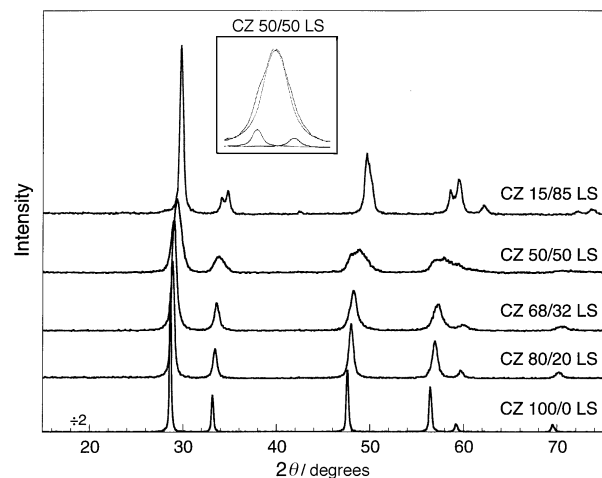


Fig. 7 XRD patterns for LS samples.

the presence of diffraction peaks corresponding to two new phases. These new phases can be indexed as solid solutions of approximate composition $\text{Ce}_{0.8}\text{Zr}_{0.2}\text{O}_2$ and $\text{Ce}_{0.2}\text{Zr}_{0.8}\text{O}_2$. From examination of the main diffraction peak in the spectra of the HS and LS series we can assign a fluorite-type cubic cation sub-lattice structure for $x > 0.5$ (CZ 100/0, CZ 80/20 and CZ 68/32) and a tetragonal one for $x \leq 0.5$ (CZ 50/50 and CZ 15/85).

In Table 2 we give the values of d_{hkl} of the peaks of highest intensity and the calculated mean crystal size (D). With the exception of CeO_2 , the mean crystal size presents values around 70–80 Å for HS oxides. Considerably higher and more heterogeneous values are found for the LS series, suggesting that thermal treatment does not affect all the HS mixed oxides in the same way. The CZ 68/32 LS and CZ 50/50 LS (for its most important diffraction peak) show relatively low values of mean crystal sizes compared to the rest of the series.

Here, we present some results of calcination experiments carried out at 1473 K for 140 h. After calcination at this temperature, all the solid solutions became a mixture of two new compositions, $\text{Ce}_{0.8}\text{Zr}_{0.2}\text{O}_2$ and $\text{Ce}_{0.12}\text{Zr}_{0.88}\text{O}_2$, approximately (Fig. 8). Even in the case of the CZ 15/85 sample, a

small peak of CeO_2 could be observed and the (111) peak is seen to shift to a higher 2θ value, corresponding to $\text{Ce}_{0.12}\text{Zr}_{0.88}\text{O}_2$. Relative peak intensities for the main diffraction peaks are reported in Table 3. It appears that both CZ 68/32 and CZ 50/50 solid solutions possess metastable structures that separate into more stable compositions upon calcination. In the case of CZ 68/32 LS this step is less favoured compared to CZ 50/50 LS and presumably requires a higher temperature. That could be the reason why no segregation was observed in the CZ 68/32 LS sample. The obtained results agree with the literature: Yao *et al.* recently reported that Ce–Zr solid solutions with Ce molar compositions of 65% and 50% present segregation into two other phases after steam-aging (hydrothermal treatment).¹⁵

By comparing the results obtained for both series we can note the following points: (i) for CZ 50/50 phase separation after calcination is observed, giving rise to two new solid solutions with approximate compositions of 80% and 20% Ce; (ii) for CZ 15/85 initial partially segregated or non-incorporated $m\text{-ZrO}_2$ disappears after the thermal treatment.

We have also calculated the values of the geometrical specific surface area, S_{XR} , from D , using the following expression:

$$S_{\text{XR}} = \frac{6 \times 10^4}{\rho D} \text{ m}^2 \text{ g}^{-1}$$

where ρ (g cm^{-3}) is the density of the sample, measured experimentally by a pycnometry technique. The values S_{XR} , as well as the differences $S_{\text{XR}} - S_{\text{BET}}$ are reported in Table 4. Specific surface areas calculated from XRD results significantly differ from the S_{BET} . Except in the case of CZ 100/0, the value of S_{XR} in the HS and LS series is higher than that of S_{BET} . This deviation can be explained by the addition of the following effects: first S_{XR} is obtained from the diffraction peak of crystallites with the initial solid solution composition, whereas S_{BET} corresponds to all the particles in the sample; then there may exist in the particles grain boundary interfaces not available to N_2 in BET measurements; finally some internal porosity associated with the grain boundary regions should be present, as indicated by the differences between the

Table 2 Values of d_{hkl} and D for $\text{Ce}_x\text{Zr}_{1-x}\text{O}_2$ HS and LS samples^a

Samples	$\text{CeO}_2(111)$ $\text{Ce}_x\text{Zr}_{1-x}\text{O}_2(111) x > 0.5$ $\text{Ce}_x\text{Zr}_{1-x}\text{O}_2(101) x \leq 0.5$		$\text{ZrO}_2(111)$	
	$d_{hkl}/\text{\AA}$	$D/\text{\AA}$	$d_{hkl}/\text{\AA}$	$D/\text{\AA}$
HS CZ 100/0	3.12	111	—	—
CZ 80/20	3.08	74	—	—
CZ 68/32	3.07	81	—	—
CZ 50/50	3.04	74	—	—
CZ 15/85	2.99	68	3.16	60
CZ 0/100	—	—	3.14	76
LS CZ 100/0	3.12	466	—	—
CZ 80/20	3.09	217	—	—
CZ 68/32	3.07	181	—	—
CZ 50/50	3.05	92	3.11	242
CZ 15/85	2.98	221	—	—

^a For comparison, $d_{hkl}/\text{\AA}$ values from JCPDS files are reported. $t\text{-ZrO}_2$: 2.995; $m\text{-ZrO}_2$: 3.165; CeO_2 : 3.124. ^b $\leq 5\%$.

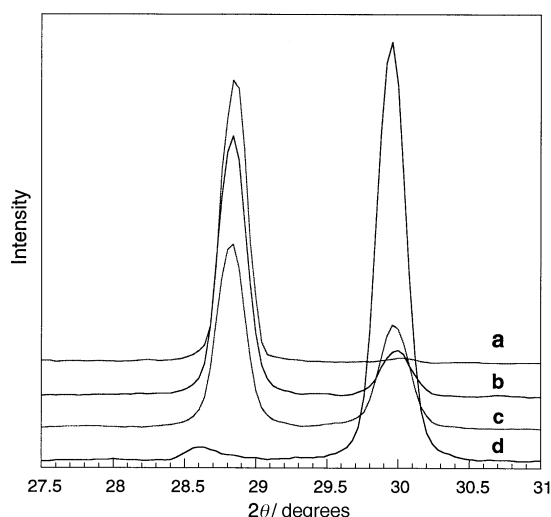


Fig. 8 XRD of HS samples calcined at 1473 K for 140 h in air; (a) CZ 80/20, (b) CZ 68/32, (c) CZ 50/50 and (d) CZ 15/85.

Table 3 Percentage of the main peak relative intensities for CZ samples calcined at 1473 K for 140 h. These intensities correspond to main peaks of solid solutions with approximately 80% and 10% Ce

Sample	$2\theta \approx 28.8^\circ$ ca. 80% CeO_2	$2\theta \approx 29.9^\circ$ ca. 10% CeO_2
CZ 100/0	—	—
CZ 80/20	100	—
CZ 68/32	87	13
CZ 50/50	65	35
CZ 15/85	4	96

Table 4 Specific surface area values calculated by means of XRD techniques and differences between values obtained using XRD and BET techniques

Sample	$S_{\text{XR}}/\text{m}^2 \text{ g}^{-1}$	$S_{\text{XR}} - S_{\text{BET}}/\text{m}^2 \text{ g}^{-1}$	$(S_{\text{XR}} - S_{\text{BET}})/S_{\text{XR}}$
HS CZ 100/0	80	−20	−0.25
CZ 80/20	126	15	0.12
CZ 68/32	115	15	0.13
CZ 50/50	133	27	0.20
CZ 15/85	154	59	0.38
LS CZ 100/0	19	−1	−0.05
CZ 80/20	43	28	0.65
CZ 68/32	58	35	0.60
CZ 50/50	107	86	0.80
CZ 15/85	48	18	0.37

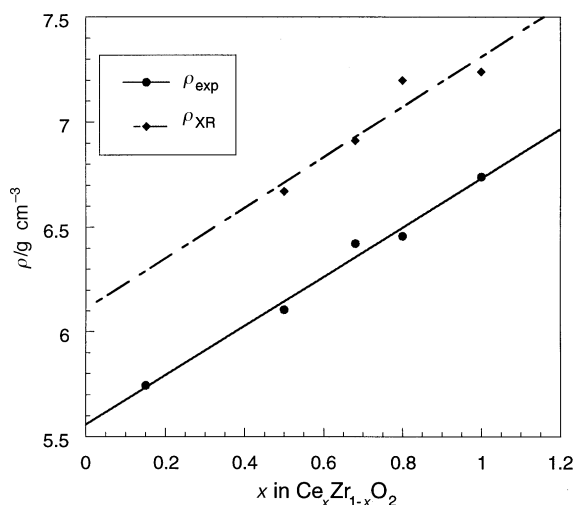


Fig. 9 Evolution of pchnometric and XRD density for CZ HS samples.

values of pchnometric and XRD calculated densities (Fig. 9). In the case of the LS series, the values of $(S_{\text{XR}} - S_{\text{BET}})/S_{\text{XR}}$ are significantly higher than those observed for the HS series, particularly in the case of CZ 50/50 LS. This must be due to the segregation of new phases, that induces a decrease in S_{BET} , while the crystallites with the initial solid solution composition do not suffer an important size increase. This is in agreement with microscopy observations, which are reported hereafter.

The unit cell parameters were calculated from d_{hkl} values and are reported in Table 5. We have applied the tetragonal relation between d_{hkl} and unit cell parameters, even in the case of cubic structure. Obviously, a and c are equal ($a/c = 1$) in the latter case. For the CZ 50/50 HS sample, peak indexation of (112) and (200) diffraction peaks was made by considering a single peak. Due to the very close position of the theoretical values and the low resolution of the diffraction peaks, it was quite difficult to identify the double peak (112)/(200) of the tetragonal structure. On the other hand for CZ 15/85 HS, peak deconvolution is not possible since, in addition to this problem, the $m\text{-ZrO}_2$ peaks overlap those of the solid solution. Therefore, for these samples we cannot distinguish the secondary double peaks corresponding to the tetragonal structure.

Observations by electron microscopy of the samples of the HS series have revealed that the mean particle size is in good

Table 5 Values of unit cell parameters for $\text{Ce}_x\text{Zr}_{1-x}\text{O}_2$ samples

Sample	$a/\text{Å}$	$a/\text{Å}$ from JCPDS	$c/\text{Å}$	$c/\text{Å}$ from JCPDS	a/c
HS CZ 100/0	5.40	5.4113	5.41	—	0.99(8)
CZ 80/20	5.35	5.3492 ^b	5.23	—	1.02(3)
CZ 68/32	5.32	5.3049 ^c	5.30	—	1.00(3)
CZ 50/50	5.28 ^a	3.7205	5.27	5.3039	1.00(2) ^a
CZ 15/85	—	3.6377	—	5.2394	—
LS CZ 100/0	5.40	5.4113	5.39	—	1.00(2)
CZ 80/20	5.36	5.3492 ^b	5.35	—	1.00(2)
CZ 68/32	5.33	5.3049 ^c	5.31	—	1.00(5)
CZ 50/50	5.24 ^a	3.7205	5.32	5.3039	0.98(5) ^a
CZ 15/85	5.13 ^a	3.6377	5.22	5.2394	0.98(3) ^a

^a This value corresponds to double tetragonal cell, $a' = a\sqrt{2}$. ^b From $\text{Ce}_{0.75}\text{Zr}_{0.25}\text{O}_2$ JCPDS file. ^c From $\text{Ce}_{0.6}\text{Zr}_{0.4}\text{O}_2$ JCPDS file.

agreement with the XRD determination, while slightly shifted by *ca.* 10 Å to higher values. In the case of the LS series, larger differences are noticed, *e.g.* 50, 80, and 160 Å for CZ 80/20, 68/32 and 50/50 compositions, respectively.

SAED patterns are obtained for all sample compositions. These were analysed and the set of lattice spacings measured from the positions of diffraction spots were compared with the crystallographic information held in databases of cubic, tetragonal and monoclinic phases. Data for pure ZrO_2 were employed, since not all the crystallographic parameters required to construct databases for the equivalent phases of Ce–Zr mixed oxides were available.

Within the range of interplanar spacings of interest in this study, the fluorite cubic structure gives rise to only three electron diffraction rings which correspond to interplanar spacings of *ca.* 3.1, 2.7 and 1.9 Å. The other two likely phases, tetragonal and monoclinic, exhibit electron diffraction rings at, or very close to, these cubic spacings, as well as additional spacings. The presence of these three former spacings in all patterns means that it is often difficult to say if a sample is purely tetragonal, for example, or if it is a mixture of tetragonal and cubic phases. The additional spacings for the tetragonal phase are at 2.1 and possibly 2.3, 3.7 (see below) and 5.3 Å (the last three being possibly active kinetic extinctions) and for the monoclinic at 2.0–2.3, 3.7 and 5.1 Å. These spacings should be treated as approximate since they will vary slightly with the Zr content of the sample. For example, the spots at 5.3 and 5.1 Å would be difficult to separate unambiguously.

Taking into account the slight contraction of the crystal lattice expected on the partial substitution of the Ce^{4+} ions by the smaller Zr^{4+} ions, simple fluorite-type SAEDs were obtained for both CZ-80/20 HS and LS samples, and for the CZ-68/32 HS. The SAED for the CZ-68/32 LS sample showed isolated spots at 2.1 Å which, in the absence of evidence for spacings at 3.7 or 5.1 Å, can best be explained by the presence of some tetragonal phase, although the possibility of a mixture of cubic and tetragonal phases cannot be excluded on the basis of TEM evidence alone. A very faint ring at *ca.* 2.1 Å was also seen in certain SAEDs for the CZ-50/50 HS sample and the patterns for CZ-50/50 LS showed similar evidence for the presence of a tetragonal phase. Finally, the SAEDs for the CZ-15/85 HS sample contain strong evidence for the presence of non-cubic phase(s). A typical pattern is presented in Fig. 10. Cubic-type diffraction rings are labelled at the bottom of the figure, while non-cubic features at 2.0–2.2, 3.7 and 5.1 Å, are arrowed. Within the accuracy of the measurements and because of the uncertainty due to the effect of varying Zr content, these data could be explained by the presence of either a monoclinic or a tetragonal phase, if we accept the presence of active tetragonal kinetic extinctions at 3.7 and *ca.* 5.3 Å. However, our dynamic calculations for the tetragonal structure predict that the 3.7 Å diffraction spots should have negligible intensity whereas, in Fig. 10, the diffraction ring at this spacing is reasonably intense. So the presence of a significant amount of monoclinic phase in the CZ-15/85 HS sample is suggested. In fact, XRD results indicate that both phases are present.

Several of these samples were studied by HREM. Micrographs were selected in which the bidimensional crystal structure was well-defined and DPPs were generated from these images by applying a Fourier-transform technique. The resulting DDPs were analysed and compared with patterns for the cubic, tetragonal and monoclinic phases for ZrO_2 . An HREM image of a CZ-50/50 HS crystal is shown in Fig. 11 with its DDP inset. The crystal presents a fluorite-type DDP. It should be remembered that the HS crystals are very small and so give rise to DDPs with less resolution than for the larger LS crystals because the sampled area is smaller. Also, the spots used to differentiate the fluorite and tetragonal patterns are kinetic extinctions, whose intensities in the DDPs

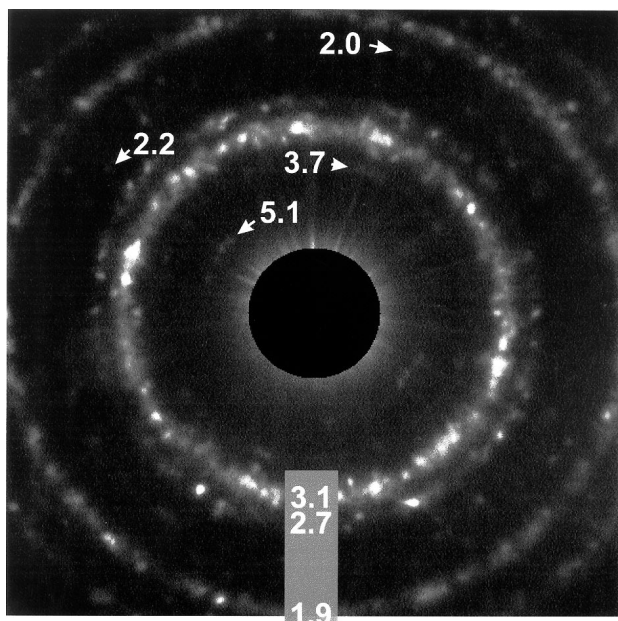


Fig. 10 Experimental SAED of the CZ-15/85 HS sample. The corresponding inter-planar spacings are given in Å. The diffraction rings indicated at the bottom of the figure at *ca.* 3.1, 2.7 and 1.9 Å are seen in samples of cubic (fluorite) structure. The fainter rings indicated by arrows cannot be explained by the cubic structure.

may depend upon the thickness and orientation of the crystal as well as the optical conditions of the microscope when the HREM image was taken. For these reasons, it is possible that a crystal with tetragonal structure might appear to have cubic structure.

Several HREM images of the CZ 50/50 LS sample contained clear evidence for crystals with tetragonal structure, such as the crystal in Fig. 12, although others gave rise to cubic-type DDPs such as that already discussed. The DDP in Fig. 12 contains what appear to be strong active $\langle 001 \rangle$ and $\langle 100 \rangle$ extinctions. However, according to our dynamic calcu-

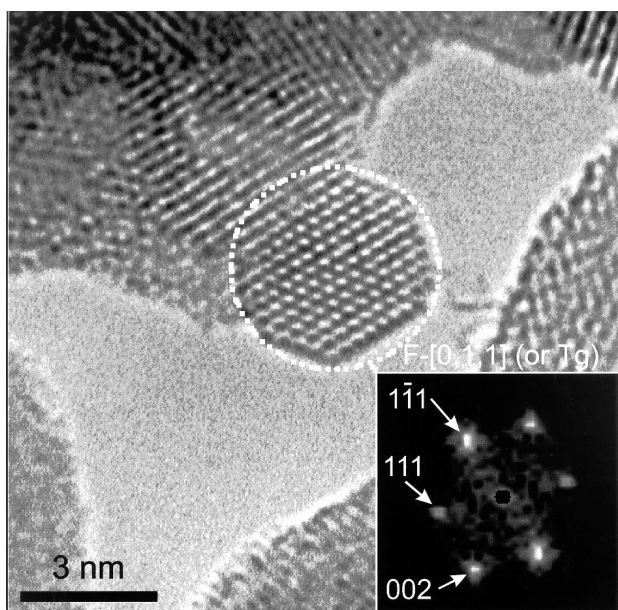


Fig. 11 HREM image of the CZ-50/50 HS sample showing part of a crystal and the corresponding DDP (inset). The DDP can be indexed to the cubic (F) structure viewed along the $[0, 1, 1]$ zone axis, as presented in the figure, or alternatively to a tetragonal (Tg) structure in which some spots are not seen (see text).

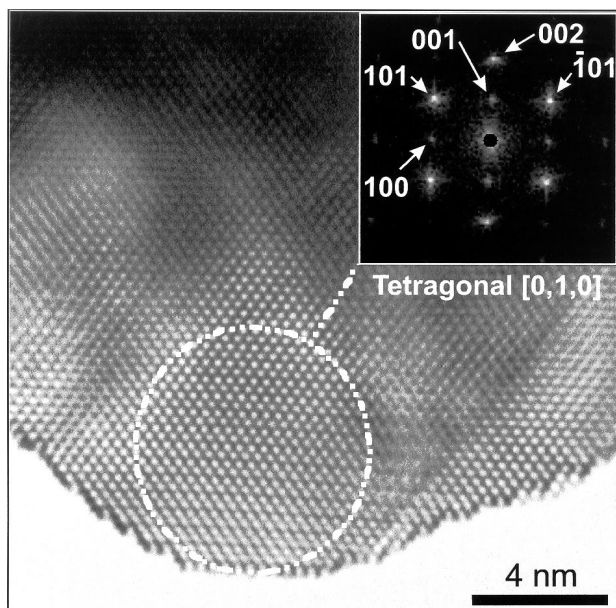


Fig. 12 HREM image of the CZ-50/50 LS sample showing part of a crystal and the corresponding DDP (inset). The DDP can be indexed to the tetragonal structure viewed along the $[0, 1, 0]$ zone axis.

lations, only the $\langle 001 \rangle$ should be visible, the $\langle 100 \rangle$ having negligible intensity. The angles measured between the spots appear to discount a monoclinic phase, which otherwise has a very similar pattern to that shown in the figure. A possible explanation is that the pattern is indeed tetragonal but that the $\langle 100 \rangle$ spots gain intensity during the imaging process at the objective lens. In this effect, second-order interactions between the $\langle 001 \rangle$ and $\langle 10\bar{1} \rangle$ spots result in the transfer of intensity to the $\langle 100 \rangle$ in the imaging plane. In this way, the presence of a tetragonal phase in CZ-50/50 LS suggested by the SAED results appears to be confirmed in the DDPs.

The CZ-15/85 HS crystal in Fig. 13 gives a DDP which can be assigned to either the $[0, 0, 1]$ or the $[1, 0, 0]$ zone axis of the monoclinic phase, depending on the assignment of the two

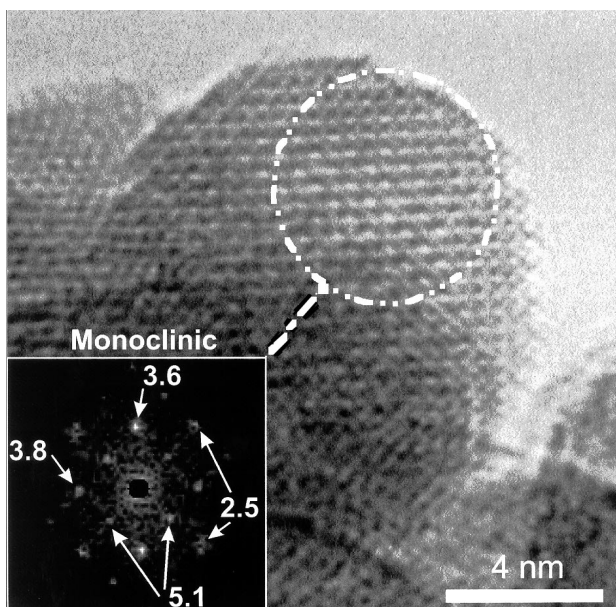


Fig. 13 HREM image of the CZ-15/85 HS sample showing a crystal and the corresponding DDP (inset). The corresponding inter-planar spacings are given in Å. The DDP can be indexed to the monoclinic structure viewed along the $[0, 0, 1]$ or $[1, 0, 0]$ zone axis (see text).

pairs of spots with spacings of 5.1 Å. According to dynamic calculations both pairs are extinctions of negligible intensity in the [1, 0, 0] zone axis, whereas only one pair would have non-negligible intensity in the [0, 0, 1] zone axis. If this is accepted, the pattern is best indexed to the [0, 0, 1] zone axis with the other pair of spots explained as second-order imaging effects, as described above. In any case, this pattern cannot be indexed to either a tetragonal or a cubic structure. Other crystals do exhibit a tetragonal structure in their DDPs and, therefore, the presence of a tetragonal phase and a monoclinic phase, assigned as *m*-ZrO₂ by XRD, is confirmed.

The literature data indicate that the phase diagram of Ce–Zr mixed oxides is quite complex. It shows a monophasic region of monoclinic symmetry for Ce molar concentration less than 20%, while for Ce contents higher than 80%, a cubic (fluorite) phase was reported.^{16–23} In the intermediate region, the true nature of the CeO₂–ZrO₂ phase diagram is still not clear,¹⁸ due to the presence of some stable and metastable phases of tetragonal symmetry.^{16–19} According to recent investigations, three different phases (*t*, *t'* and *t''*) can be distinguished on the basis of XRD and Raman characterization.^{18,20–22} The *t* form is a stable one, formed through a diffusion phase decomposition, *t'* is obtained through a diffusionless transition and it is metastable, and *t''* is intermediate between *t'* and cubic structures. In the *t''* phase, the cation sub-lattice remains cubic, the phase being distinguished from the cubic phase only because of a displacement of the oxygen ions from their ideal fluorite sites.^{20,21} However these phases have been prepared after annealing at temperatures above 1000 °C, which is very different from the samples under study, especially from the point of view of the crystallite size. The contribution of the surface energy to the total energy of these phases should not be neglected when considering their thermodynamic stability.

Raman spectra of the oxide samples are collected in Fig. 14 and 15. The main difference between the HS and LS series is basically that the peaks in the spectra become narrower for the LS samples due to crystallite growth, which takes place during their preparation from the HS samples. In general, the Raman spectra support well the XRD analysis for the Ce–Zr solid solutions. For example, the comparison of CZ 0/100 HS [Fig. 14(f)], whose spectrum shows the typical bands of *m*-ZrO₂, with CZ 15/85 HS confirms the presence of a monoclinic phase (additional peaks at 259 and 145 cm⁻¹), as was established in Fig. 6 and confirmed by microscopy. Upon calcination to obtain the LS sample [Fig. 15(e)] only the peaks attributable to the tetragonal solid solution are detected. Note

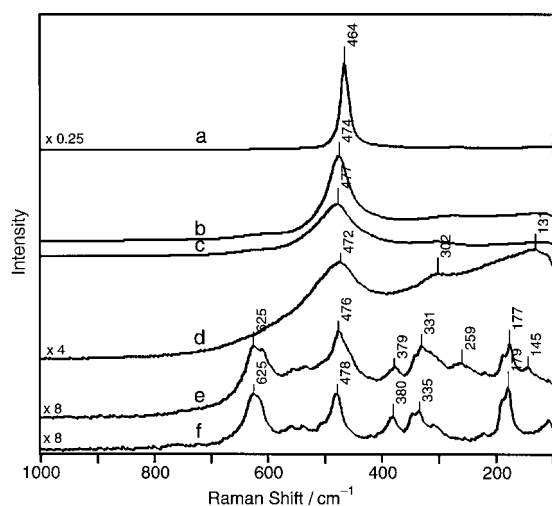


Fig. 14 Raman spectra for (a) CZ 100/0, (b) CZ 80/20, (c) CZ 68/32, (d) CZ 50/50, (e) CZ 15/85 and (f) CZ 0/100 HS samples.

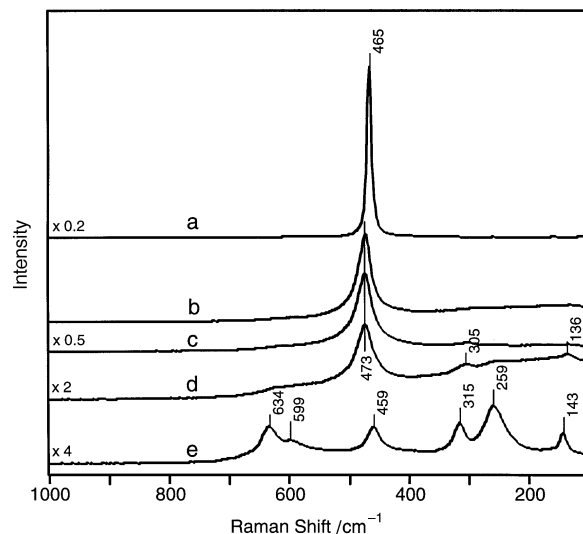


Fig. 15 Raman spectra for (a) CZ 100/0, (b) CZ 80/20, (c) CZ 68/32, (d) CZ 50/50 and (e) CZ 15/85 LS samples.

the shoulder at ca. 465 cm⁻¹ in the CZ 15/85 HS, which also disappears after calcination, indicating that a small amount of CeO₂, below the XRD detection limit, may be present in the HS sample and is incorporated in the lattice upon calcination. The peaks located at around 300, 130–140 cm⁻¹ and, for CZ 15/85, ca. 259 cm⁻¹ are characteristic of a tetragonal phase.²² The first two are observed in spectra for both HS and LS samples of compositions CZ 15/85 and CZ 50/50. These peaks are less intense in the spectra of the CZ 68/32 HS and LS samples [Fig. 14(c) and 15(c)], which could indicate that these samples contain both cubic and *t''* phases.

Bringing together the results from XRD, TEM and Raman studies, it is possible to summarise the phases for which there is good evidence by sample composition (Table 6).

Surface properties

In order to complete the characterisation of these oxides, we included also information from methanol adsorption followed by FTIR spectroscopy. Preliminary experiments showed that pyridine and CO adsorptions hardly distinguish between Ce⁴⁺ and Zr⁴⁺ adsorption sites. By contrast, methanol gives interesting results, as reported below. CH₃OH was adsorbed over the clean surface of the activated samples. The methanol adsorption is dissociative over both zirconia^{24,25} and ceria^{26,27} surfaces, and methoxy species formed can be either on-top or bridged over two or three cation sites. In the case of zirconia, bands have been reported at 1163 and 1070 cm⁻¹ [see Fig. 16(a), on-top and doubly bridging species], whereas on ceria they are situated at 1107 (on-top), 1063 with a shoul-

Table 6 Phase assignment in the CZ HS and LS samples

Sample	HS	LS
CZ 100/0	<i>c</i>	<i>c</i>
CZ 80/20	<i>c</i>	<i>c</i>
CZ 68/32	<i>t''</i> (and <i>c</i> ?)	<i>t''</i> (and <i>c</i> ?)
CZ 50/50	Tetragonal	Tetragonal (+ Ce _{0.8} Zr _{0.2} O ₂ , Ce _{0.2} Zr _{0.8} O ₂)
CZ 15/85	Tetragonal and <i>m</i>	Tetragonal

*Tetragonal' in the table indicates inclusion of *t'* and/or *t* phase(s).

der at 1042 cm^{-1} (doubly bridging) and 1014 cm^{-1} (triply bridging methoxy species), as shown in Fig. 16(f). On mixed oxides, if doubly bridged species with a mixed character, *i.e.*



occur, the corresponding $\nu(\text{OC})$ band is expected at *ca.* $1070\text{--}1060\text{ cm}^{-1}$ and it is therefore very difficult to differentiate from those due to



and



species.

Nevertheless, all the bands corresponding to methanol dissociative adsorption on either cerium or zirconium ions on the mixed oxides present a slight but regular shift of the peaks position (few cm^{-1}) with respect to the bands for pure samples. The band near 1100 cm^{-1} shows a monotonic downward shift from 1106 (pure CeO_2) to 1102 cm^{-1} (CZ-50/50-HS sample), while the band near 1150 cm^{-1} shows a more important shift from 1163 (CZ-0/100-HS) to 1149 cm^{-1} (CZ-80/20-HS), being thus sensitive to the different surrounding ions at the surface. This is in favour of the formation of a solid solution.

The surface composition will be deduced from the relative intensity of the $\nu(\text{OC})$ vibrations of $\text{CH}_3\text{--O--Zr}$ and $\text{CH}_3\text{--O--Ce}$ on-top species.

The corresponding $\nu(\text{OC})$ bands at 1163 and 1107 cm^{-1} , respectively, are sufficiently resolved to determine their relative intensity even without any spectrum deconvolution. The $\nu(\text{OC})$ range of the mixed oxides spectra after methanol adsorption is reported in Fig. 16(b) and (c). It is clear that the 1163 cm^{-1} band intensity decreases (whereas that at 1107 cm^{-1} increases) when the cerium content increases.

If we consider the intensity of the band near 1163 cm^{-1} (Fig. 17), it varies almost linearly with the zirconia content. Assuming that for methoxy species adsorbed on zirconia the

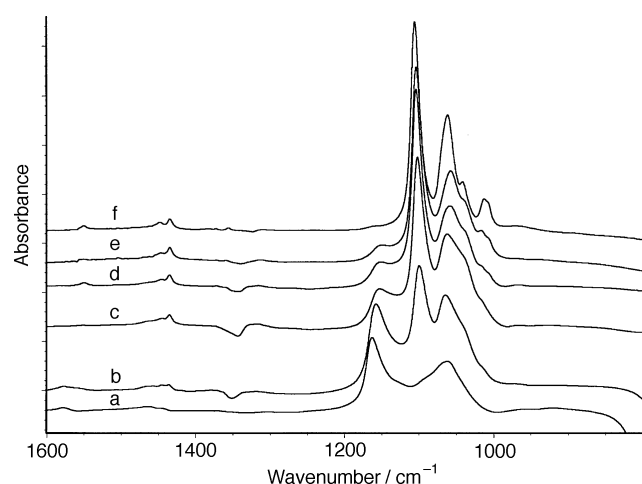


Fig. 16 FTIR spectra of the surface methoxy species formed by methanol dissociative adsorption over (a) CZ 0/100, (b) CZ 15/85, (c) CZ 50/50, (d) CZ 68/32, (e) CZ 80/20 and (f) CZ 100/0 HS samples, after evacuation at 373 K in the C—O stretching region.

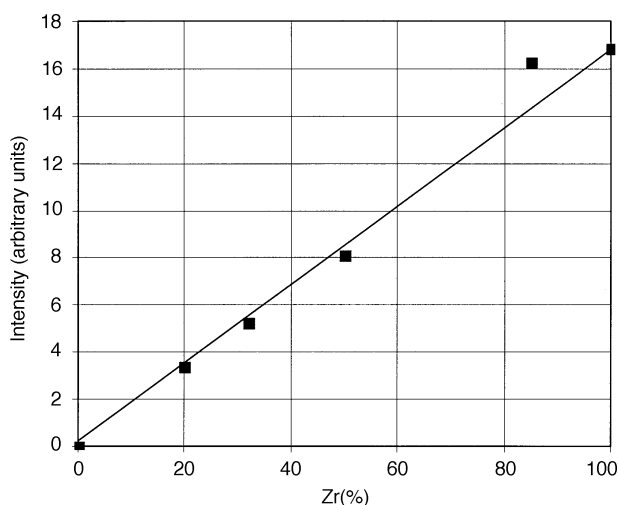


Fig. 17 Intensity of the IR $\nu(\text{OC})$ band at 1150 cm^{-1} due to on-top methoxy species adsorbed on Zr^{4+} ions.

ratio between on-top species and bridging ones is independent of composition, this implies that the surface composition is strictly correlated to the bulk one.

Conclusions

$\text{Ce}_x\text{Zr}_{1-x}\text{O}_2$ ($0 < x < 1$) mixed oxides have been studied and we have presented a complete textural and structural report. Initial samples (HS series) present high specific surface area values, *ca.* $100\text{ m}^2\text{ g}^{-1}$ and no microporosity. The thermal treatment of HS samples produces significant textural and structural changes. Specific surface areas decrease to *ca.* $15\text{--}30\text{ m}^2\text{ g}^{-1}$ and pore size distribution moves to higher diameters. In no case is microporosity observed.

In order to obtain a precise definition of the structure of high and low specific surface area samples, we have brought together information from XRD, electron microscopy and Raman spectroscopy techniques.

The starting (HS) mixed oxides present solid-solution XRD patterns, except in the case of the CZ 15/85 HS sample. It is clear that CZ 15/85 HS is a mixture of *m* and tetragonal phases and that the *m*-phase, identified as *m*- ZrO_2 by XRD, disappears during the thermal aging preparation of the corresponding LS material. The HS samples with $\text{Ce} \leq 50\%$ are seen to contain the tetragonal phase in XRD whilst tetragonal phases are seen in Raman spectroscopy for $\text{Ce} \leq 68\%$. Because of the different sensitivities of the two techniques to O ion displacements, this suggests that *t'* [in which the cation sub-lattice remains cubic but the O ions are displaced from their fluorite (cubic) position] is present in CZ 68/32 HS. CZ 50/50 HS would then best be assigned as *t'* and/or *t*. Both CZ 80/20 HS and LS appear to be cubic. This is in agreement with TEM which also provide evidence of tetragonal phase in CZ 68/32 LS, CZ 50/50 (HS and LS) and CZ 15/85 (HS and LS).

In addition, XRD results suggest that partial demixing occurred during the thermal aging preparation of the CZ 50/50 LS sample forming two new phases of approximate composition $\text{Ce}_{0.8}\text{Zr}_{0.2}\text{O}_2$ and $\text{Ce}_{0.2}\text{Zr}_{0.8}\text{O}_2$. This analysis was supported by further experiments in which samples of all compositions separated completely into two new phases of estimated formulae $\text{Ce}_{0.80}\text{Zr}_{0.20}\text{O}_2$ and $\text{Ce}_{0.12}\text{Zr}_{0.88}\text{O}_2$ on prolonged aging at 1473 K .

Complementary results have been obtained from FTIR spectroscopy of adsorbed methanol. Consideration of these results indicates that the mixed oxides present an overall com-

position at the surface in accordance with the values for the bulk. Thus the absence of CeO₂ or ZrO₂ enrichment at the surface is implied.

On the basis of the present characterization of HS and LS mixed oxides, future attention will be dedicated to investigation of the thermal stability at high temperatures, both from the point of view of specific surface area and crystalline structure. This should give important insight for the use of such systems as TWC promoters.

Acknowledgements

Financial support has been received from the TMR Program of the European Commission (CEZIRENCAT Project, European Contract FMRX-CT-96-0060). G.C., H.V., E.F., M.D. and R.T.B. would like to acknowledge their TMR Program fellowships. Prof. M. Graziani, University of Trieste is acknowledged for helpful discussion.

References

- 1 B. Harrison, A. F. Diwell and C. Hallett, *Platinum Metals Rev.*, 1988, **32**, 73.
- 2 J. C. Summers and S. A. Ausen, *J. Catal.*, 1979, **58**, 131.
- 3 H. C. Yao and Y. F. Yu Yao, *J. Catal.*, 1984, **86**, 254.
- 4 P. Fornasiero, G. Balducci, J. Kašpar, S. Meriani, R. di Monte and G. Graziani, *Catal. Today*, 1996, **29**, 47.
- 5 T. Murota, T. Hasegawa, S. Aozasa, H. Matsui and M. Motoyama, *J. Alloys Comp.*, 1993, **131**, 298.
- 6 B. K. Cho, *J. Catal.*, 1991, **131**, 74.
- 7 Y. Zhang, A. Andersson and M. Muhammed, *Appl. Catal. B*, 1995, **6**, 325.
- 8 T. Murota, T. Hagesawa, T. Aozasa, H. Matsui and M. Motoyama, *J. Alloys Comp.*, 1993, **191**, 298.
- 9 P. Fornasiero, R. di Monte, G. R. Rao, J. Kašpar, S. Meriani, A. Trovarelli and M. Graziani, *J. Catal.*, 1995, **151**, 168.
- 10 J. Cuif, G. Blanchard, O. Touret, M. Marczl and E. Quéméré, SAE Tech. Pap. Ser. 969106, 1996.
- 11 M. Pijolat, M. Prin, M. Soustelle, O. Touret, and P. Nortier, *J. Chem. Soc., Faraday Trans.*, 1995, **91**, 3941.
- 12 C. Janvier, M. Pijolat, F. Valdivieso, M. Soustelle and C. Zing, *J. Europ. Ceram. Soc.*, 1998, **18**, 1998 1331.
- 13 S. J. Gregg and K. S. W. Sing, in *Adsorption, Surface Area and Porosity*, Academic Press, London, 1991.
- 14 E. P. Barrett, L. G. Joyner and P. H. Halenda, *J. Am. Chem. Soc.*, 1951, **73**, 373.
- 15 M. Yao, R. J. Baird, F. W. Kunz and T. E. Hoost, *J. Catal.*, 1997, **166**, 67.
- 16 E. Tani, M. Yoshimura and S. Somiya, *J. Am. Ceram. Soc.*, 1983, **66**, 506.
- 17 P. Durán, M. González, C. Moure, J. R. Jurdo and C. Pascal, *J. Mater. Sci.*, 1990, **25**, 5001.
- 18 M. Yashima, K. Morimoto, N. Ishizawa and M. Yoshimura, *J. Am. Ceram. Soc.*, 1993, **76**, 1745.
- 19 S. Meriani, *Mater. Sci. Eng. A*, 1989, **109**, 121.
- 20 M. Yashima, K. Morimoto, N. Ishizawa and M. Yoshimura, *J. Am. Ceram. Soc.*, 1993, **76**, 2865.
- 21 M. Yashima, H. Arashi, M. Kakihana and M. Yoshimura, *J. Am. Ceram. Soc.*, 1994, **77**, 1067.
- 22 M. Yashima, T. Hirose, S. Katano, Y. Suzuki, M. Kakihana and M. Yoshimura, *Phys. Rev. B*, 1995, **51**, 8018.
- 23 S. Meriani, *Mater. Sci. Eng.*, 1985, **71**, 369.
- 24 D. Bianchi, T. Chafik, M. Khalfallah, S. J. Teichner, *Appl. Catal. A*, 1995, **123**, 89.
- 25 M. Bensitel, V. Moravek, J. Lamotte, O. Saur and J. C. Lavalley, *Spectrochim. Acta*, 1987, **12**, 1487.
- 26 A. Badri, C. Binet and J. C. Lavalley, *J. Chem. Soc., Faraday Trans.*, 1997, **93**, 1159.
- 27 C. Binet, A. Badri and J. C. Lavalley, *J. Phys. Chem.*, 1994, **98**, 6392.

Paper 8/07680D